PROGRESS TOWARDS ECHO-SEEDING IN THE FLASH ORS SECTION

Kirsten Hacker*, Shaukat Khan, Technische Universitaet Dortmund
Holger Schlarb, DESY Hamburg
Peter Van der Meulen, Peter Salen, Stockholm University
Armin Azima, University of Hamburg
Gergana Angelova Hamberg, Volker Ziemann, Uppsala University

Abstract

This is a report on the progress towards commissioning the hardware for echo-seeding experiments in the FLASH Optical Replica Synthesizer (ORS) section in Jan 2012. It is anticipated that echo-seeding in the ORS section can produce harmonics of the 270 nm seed laser wavelength, generating seeded FEL radiation in the sFLASH undulators with wavelengths ranging from 10 nm to 30 nm. It is planned to operate this experiment parasitically and continuously throughout 2012, requiring a few shifts of dedicated beam time only for initial calibration of alignment references. The technical layout, components, and tuning procedures involved in this experiment are described and the expected difficulties are specified.

INTRODUCTION

Echo-Enabled Harmonic Generation (EEHG), also known as echo-seeding is a technique which was proposed in 2008 [1,2] that calls for the co-propagation of an electron bunch and laser pulse through an -undulator, chicane, undulator, chicane- series. Through interaction with a seed laser, the electron beam develops an energy modulation in the first undulator which is then over-compressed in the first chicane, creating a charge density modulation in longitudinal phase space consisting of horizontal or diagonal stripes of high-charge density separated by low-charge density regions. The electron bunch is then modulated again in the second undulator and compressed in the second chicane, resulting in vertical stripes of charge with a periodicity equal to a harmonic of the seed laser wavelength.

EEHG schemes have recently been proposed for several seeded FELs [3-5] and proof-of-principle experiments at two facilities have been able to generate low-harmonics of the seed laser wavelength [6,7]. The proposed schemes all call for a large, 1-10 mm R_{56} in the first chicane and when one sees that the FLASH ORS section chicanes can only achieve a maximum R_{56} of ~130 μm, one is initially inclined to reject the possibility of doing EEHG with this section, even though an ideal laser is available and the – undulator, chicane, undulator, chicane – layout looks appropriate. However, by replacing the FLASH correctors with HERA correctors, one can achieve a maximum R_{56} of 700 μm in the first chicane of the ORS section and while this is somewhat small, the available laser power is large and EEHG up to the 20th harmonic can still be pursued [10].

*kirsten.hacker@desy.de

To inject the seed laser required by EEHG, a new laser-transport line will be constructed during the last 3 months of 2011. The frequency tripler, polarization delay control, telescoping, and steering of this laser beam will be described in detail in this paper.

CHICANE PROPERTIES

The minimum wavelength that can be achieved with EEHG in the ORS section is eventually determined by the maximum R_{56} in the first chicane. The maximum R_{56} is determined by the corrector strength, the chicane length and the vacuum chamber radius. The effective vacuum chamber radius is ~15 mm and for an effective chicane length of 1.5 m, the maximum $R_{56,}$ as limited by the vacuum pipe, would be 600 μm. The limitations on the R_{56} due to the strength of the FLASH correctors which are currently installed are more severe: R_{56} < 130 μm for a 1 GeV beam energy. If, however, the FLASH correctors are replaced with HERA correctors, the R_{56} limitation of the chicane is increased to 700 μm, limited by the 15 mm effective radius of the 17.5 mm radius vacuum chamber.

A model of the chicane before and after the replacement of the correctors is shown below in Fig. 1.

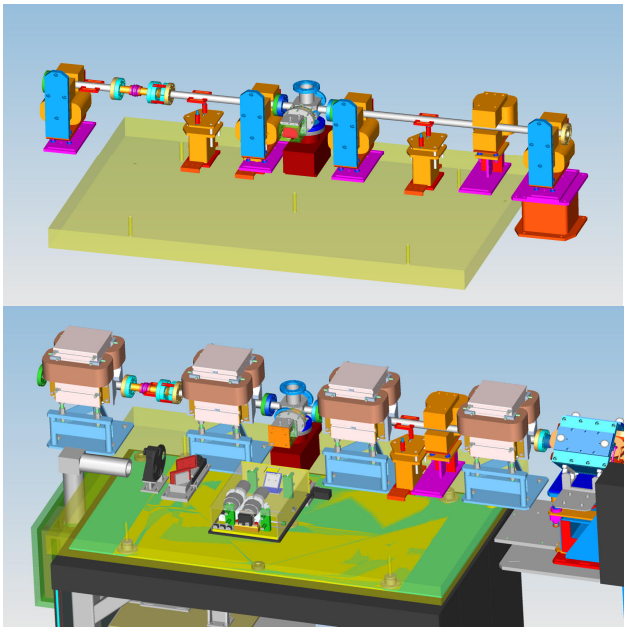

Figure 1: Model of the first ORS chicane before (top) and after (bottom) the replacement of the FLASH correctors with stronger HERA correctors

Two flanges on the left side of the drawing will be moved by about a centimeter. The toroid between the two correctors on the left will also be moved by about a centimeter. These adjustments required the manufacture and installation of two short sections of vacuum pipe. New magnet support structures were also manufactured.

Calculations of the R_{56} limitations for the FLASH correctors (40 mm gap) which are installed in the present chicane are shown in Table 1, alongside calculations of the limitations of the chicane with HERA correctors (40 mm gap). The HERA correctors will fit in the allocated space but they typically have a gap of 80 mm, so they needed to be outfitted with 20 mm "pole-shoes" to reduce the gap and increase their strength. These pole-shoes have been manufactured, measured and sorted with an eye to making the chicane as symmetrical as possible [11].

@1GeV	FLASH correctors	HERA correctors
Max Current	3.5 A	3.5 A
Pole Gap	40 mm	40 mm
Magnetic field	300 mT	280 mT
Physical length	100 mm	300 mm
Deflection Angle	9 mrad	30 mrad
Dist. btw. Dipoles	0.75 m	0.345 m
Dispersion (R_{56})	130 μm	980 μm

Table 1: Comparison of possible chicane dipoles at 1 GeV. With the HERA correctors, the maximum R_{56} of the chicane will be increased to the 700 μm limit imposed by the radius of the vacuum pipe.

With smaller magnets it is possible to make finer adjustments to the steering of a beam, but while the replacement of the smaller correctors in the first ORS chicane with larger correctors does remove one digit of steering precision, the second ORS chicane retains the original, smaller magnets, maintaining the fine steering into the sFLASH undulators. A diagram of the section, with dimensions is shown below in Fig. 2.

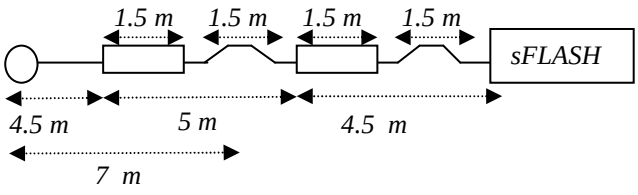

Figure 2: The dimensions of the ORS section. The laser injection point is shown on the left, followed by the ORS section undulator, chicane, undulator, chicane series. The first of the sFLASH undulators is drawn on the right. Each ORS undulator and chicane is approximately 1.5 meters long. The distance from the injection point to the middle of the first ORS chicane is 7 meters.

NON-LINEAR PHASE SHIFT

The beam size must be made as large as possible when it travels through windows and air. This is due to the requirement that the electric field in refractive materials should be kept low. If the electric field of the pulse in a refractive material is high, the nonlinear phase shift will be high, potentially distorting the pulse spatially or generating damaging hot-spots through self-focusing. The nonlinear phase shift, or B-integral, is given by,

$$B = \frac{2\pi}{\lambda} \int n_2 \ell(z) dz \,, \qquad (1)$$

Where λ is the wavelength, n_2 is the nonlinear index quantifying the Kerr nonlinearity, and $\ell(z)$ is the optical intensity along the beam axis. For values above 1, pulse distortions begin to occur and for values between 3-5, self-focusing can occur. Self-focusing occurs because the refractive index becomes larger in the areas where the intensity is higher, creating a focusing density profile which potentially leads to the collapse of a beam on itself. Below the self-focusing threshold, it tends to generate an intensity dependent curvature of the wavefronts in the central portion of the beam. For air, $n_2 \approx 4 \cdot 10^{-23}$ m^2/W for λ = 800 nm [15]. For silica, $n_2 \approx 2.4 \cdot 10^{-20}$ m^2/W [16]. The cumulative B-integrals for all dispersive materials must be less than one for any given pulse. For example, a 130 fs (FWHM), 30 mJ Gaussian pulse of 800 nm light with a diameter of 16 mm (FWHM) can travel through 3 meters of air and 3 mm of silica before the B-integral approaches one.

SEED TRANSPORT

The existing seed laser system produces 800 nm light with a pulse energy of up to 30 mJ and a pulse length which can be adjusted between 30 fs and more than a picosecond. For the echo-seeding experiment, we intend to adjust the compressor in such a way that the pulses will have a negative chirp of approximately -90 THz/ps and a duration of about 130 fs FWHM.

The laser sits on an optical table in a laser lab adjacent to the accelerator tunnel, together with the pulse compressor followed by a Galilean telescope which will expand the beam diameter from 6.5 mm (FWHM) to 16 mm (FWHM). This makes the B-integral over the 3 meters of air and 3 mm of glass prior to the vacuum acceptable for pulse energies of up to 30 mJ.

After the telescope the beam is periscoped down through a hole in the floor into a pit in which the new, 10^{-6} mbar evacuated laser transport line begins. The window at the entrance to the vacuum will be followed by 8 meters of evacuated DN50 ISO-KF pipe, ending in the accelerator tunnel. The locations of the lab, tunnel, and pipe are depicted below in Fig. 2.

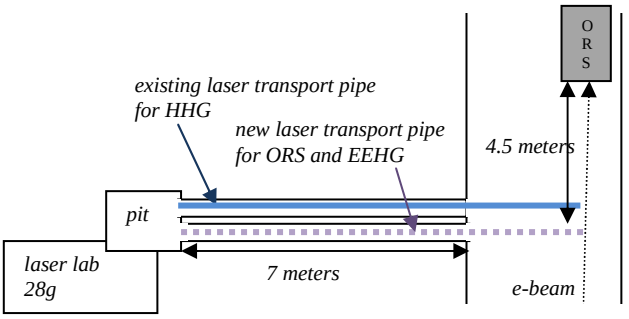

Figure 2: Location of new laser transport line with respect to the accelerator tunnel, laser table and first ORS undulator.

After the 8 meters of vacuum pipe, the laser beam will enter the first of two 70x30x30 cm evacuated boxes installed in the accelerator tunnel. These boxes are followed by another segment of pipe and two flange mounted steering mirrors, the last of which reflects the laser beam onto the electron beam axis. The dimensions of the vacuum pipes, boxes and flange mounted mirrors in the tunnel are depicted below in Fig. 3. The electron beam direction is into the page and the last of the steering mirrors is located in the upper right hand corner directly in front of the cylinder which is frequently referred to as the sFLASH mirror chamber.

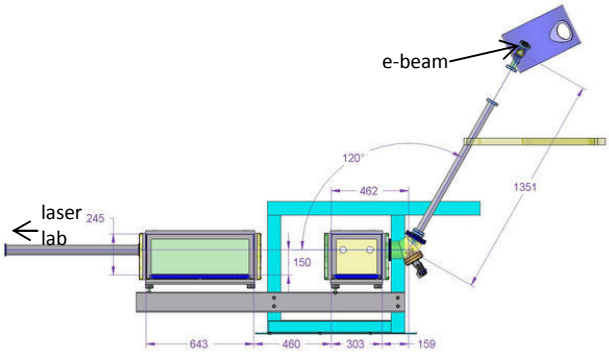

Figure 3: Side-view and dimensions of evacuated laser transport line in the accelerator tunnel. Dimensions are given in millimeters. The electron beam direction is into the page in the upper-right corner.

The evacuated boxes will contain optical breadboards on which a frequency tripler, a polarization controller, a Galilean telescope, and two motorized steering mirrors will be mounted. Two more motorized steering mirrors are mounted in vacuum flanges following the boxes. A window directly after the last box marks the transition between the high vacuum (10^{-6} mbar) of the laser transport line and the ultra-high vacuum (10^{-9} mbar) of the accelerator. The optics in these boxes will be assembled in a clean room before they are installed in the tunnel. Once they are in the tunnel it will be possible to access the optics by opening one of the panels on the box. Clean-room level dust control is not required, but special care must be taken to avoid introducing oil into the system. The layout of these components is depicted in Fig. 4.

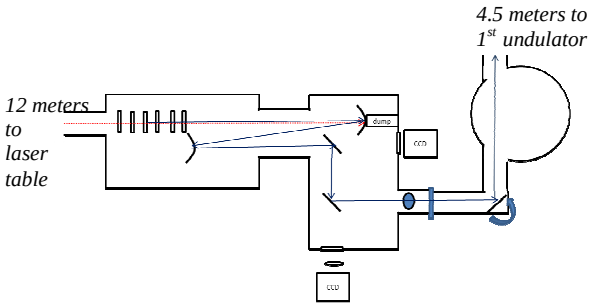

Figure 4: Top-view of optics in the accelerator tunnel. Frequency tripler and polarization control optics are followed by a Galilean telescope and four motorized steering mirrors.

The telescope in the laser lab will be slightly misaligned in order to create a 10 mm (FWHM) waist in the 21 mm diameter aperture tripler which sits 12 meters away, in vacuum. This beam diameter is large enough to avoid nonlinear phase shift problems in the transmission through the 4 mm thick alpha-BBO crystal in the tripler and the two 1 mm thick waveplates after the tripler.

The telescope after the tripler will generate a focus in between the ORS undulators. For a 100 fs (FWHM), 1.6 mJ Gaussian beam, a 740 μm (FWHM) waist is consistent with the ~$1 \cdot 10^{12}$ W/cm^2 intensity required in the undulators. It would also create a 2.5 mm (FWHM) spot size and a B-integral of 0.35 at the 1 mm thick window into the UHV. A smaller waist would increase the spot size at the window but it would degrade the peak power in the undulators. A larger waist would do the reverse. It is known that the electron bunch diameter must be at least 3 times smaller than the laser beam diameter in order for the electron bunch to experience a more flat wavefront. Wavefront control and optimization of the laser focus will be decribed in more detail in a subsequent section.

The standard window thickness for a 1" window is 3 mm, a value which is deemed safe for a scratched fused silica window under the influence of a 4 millibar pressure wave. Because we will use a high-quality crystalline quartz window which is ten times stronger than high-quality fused-silica and because the window is at the interface between high and ultra-high vacuum, we believe that a 1 mm thickness should be more than sufficient. If the custom window which we have ordered begins to leak, it can be replaced on short-notice with a standard, 3 mm thick window.

FREQUENCY TRIPLER

The seed pulses at 267 nm will be produced in two steps. First, the 800 nm light pulses will be frequency doubled in a beta-BBO non-linear optical crystal (cut at 29 degrees) to obtain pulses centered at 400 nm. In a second non-linear beta-BBO crystal (cut at 44 degrees) the 405 nm and 811 nm pulses are mixed in order to obtain the desired pulses with a center wavelength of 267 nm. Both non-linear optical crystals have a thickness of 0.2 mm and

for both frequency conversion processes, so-called Type I (o + o → e) phase-matching is used.

The polarization of the 400 nm pulses produced in the first non-linear optical crystal is orthogonal relative to the polarization of the 800 nm fundamental. In the subsequent mixing step, parallel polarizations are required and before entering the second non-linear optical crystal, the polarization of the 800 nm pulse is rotated by a properly oriented dual-wavelength, zero-order waveplate. This waveplate acts a ½-waveplate for the 800 nm pulse and a full waveplate for the 400 nm pulse.

In order to (pre)compensate for the group-delay between the 400 nm and 800 nm pulses induced by the various optical components, a 4 mm thick alpha-BBO (cut at 70 degrees) crystal is inserted between the first non-linear BBO crystal and the dual-wavelength waveplate. The optical properties of alpha-BBO are very similar to that of the more familiar beta-BBO, but due to its symmetric crystal structure, frequency-doubling and sum frequency generation processes do not occur in an alpha-BBO. As shown in Fig. 5, a simple rotation of the alpha-BBO crystal allows us to accurately and precisely vary the time-delay between the arrival of the 400 nm and 800 nm pulses at the second non-linear mixing crystal over a range of several hundreds of femtoseconds. This is important for the optimization of the yield of the third harmonic.

Both frequency conversion processes in the tripling unit have been simulated using SNLO software [17]. In the first step the second harmonic is produced with a yield of, typically, 30%. With a pulse duration of about 80 fs FWHM, the 400 nm pulse produced is slightly shorter than the original 800 nm pulse of 130 fs FWHM. The 800 nm fundamental pulse gains non-Gaussian character and broadens to about 180 fs FWHM directly after the crystal, largely because the conversion efficiency is highest close to the center of the pulse. In frequency space, the 400 nm and 800 nm pulses have similar widths (FWHM), but the chirp of the second harmonic increases to about -165 THz/ps, whereas the average chirp of the fundamental decreases to about -65 THz/ps.

Due to a combination of ordinary (linear) dispersion, self-phase modulation and cross-phase modulation in the dual-wavelength waveplate and the alpha-BBO delay crystal, the 2nd-harmonic pulse is strongly compressed to about 60 fs FWHM before it enters the final non-linear mixing crystal. Concomitantly, this pulse acquires a slight positive chirp. On the other hand, the 800 nm pulse passes through these optical components with relatively minor changes. The marked compression and the positive chirp of the 400 nm pulse greatly enhance the yield of the frequency mixing process in the final non-linear optical crystal and the SNLO software predicts a yield of close to 20% for the 3rd-harmonic at 267 nm. The computed duration of the 267 nm pulse produced is just under 100 fs FWHM and its spectral width is approximately 6 THz (or 1.5 nm) FWHM. The time-bandwidth product of about 0.6 is relatively close to that of a transform limited Gaussian pulse and the chirp is small. The temporal and spectral profiles of the 3rd-harmonic pulse are presented in Fig. 5, together with a schematic representation of the tripling unit. The crystal dimensions and the mechanical rotations required for each crystal are listed below. The rotation stages and goniometers used to rotate and tilt the crystals will not be motorized. The tripler will be aligned in the laser lab and then installed as a unit in the tunnel on a tip-tilt platform.

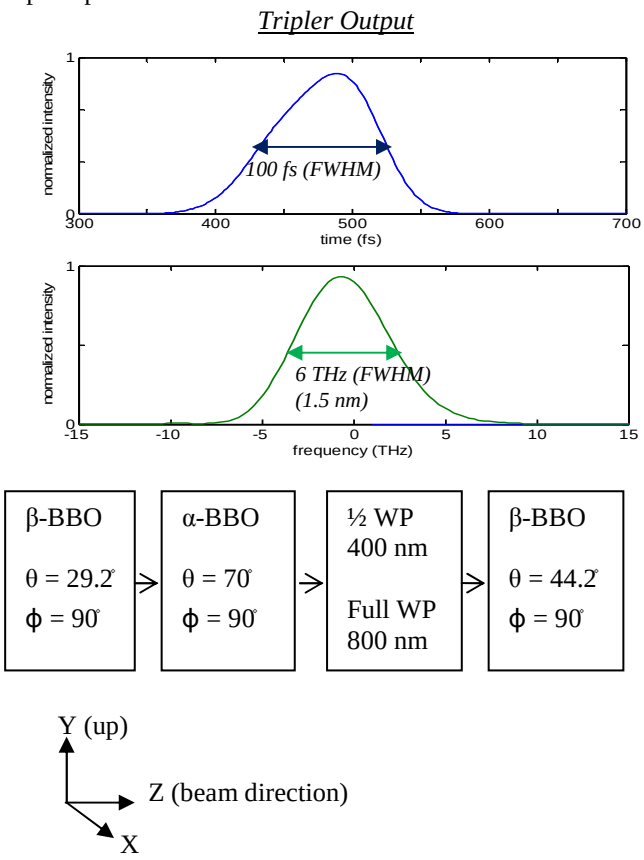

Rotation of crystal about axis:

Y	X	Z	Y
Crystal dimensions (mm):			
21x21x0.2	30x21x4	21x21x1	21x21x0.2

Figure 6: Temporal and spectral profiles of the 3rd-harmonic pulse generated with SNLO software [12] (top). Crystal properties and required mechanical rotations (bottom).

The calculated values for the average values of M_{x2} and M_{y2} of the 266.7 nm pulse are 1.12 and 1.14, respectively, but the actual values vary significantly across the temporal or spectral envelope of the pulse. Likewise, the pulse is tilted with maximum tilt close to the center of the pulse. Summarizing the results of the SNLO calculations, we can conclude that for this particular tripling configuration the simulations predict the production of the third harmonic in rather high yield, higher than the 10-15% yields quoted for commercially available triplers. Moreover, both the temporal-spectral and the spatial The calculated values for the average M_{x2} and M_{y2} of the 270

nm pulse are 1.12 and 1.14, respectively, but the actual values will vary significantly across the temporal or spectral envelope of the pulse. Likewise, the pulse is tilted with maximum tilt close to the center of the pulse.

Summarizing the results of the SNLO calculations, we can conclude that for this particular tripling configuration the simulations predict the production of the 3rd-harmonic with a rather high-yield, higher than characteristics of the 3rd-harmonic pulse appear promising. However, a number of effects, such as self-focusing in the relatively thick alpha-BBO delay crystal have not been included in the simulations, and one should leave open the possibility that, in practice, both the yield and the optical quality of the pulse are worse than suggested by the simulations. If it is found that lower input power levels produce a better output beam, it might be possible to replace the alpha-BBO with a thinner calcite crystal. This would be better, due to the thinness of the crystal, but worse due to the lower damage threshold of calcite. It is well known that the spatial quality of the input pulse has a particularly strong influence on the tripler efficiency and that is why it is anticipated that the adaptive mirror which will be used to tune the wavefront of the 800 nm pulse will be particularly beneficial.

SYNCHRONIZATION

Because 25 fs (rms) synchronization of the electron bunch with the Master Laser Oscillator (MLO) is accessible through electron bunch arrival-time feedbacks [18], when an optical cross-correlator for the seed laser is commissioned, this will lock the seed laser to the MLO with few-femtosecond accuracy [19], giving seeding and slicing schemes access to 25 fs (rms) synchronization with the electron bunch. With the existing RF laser phase-lock loop used to synchronize the seed laser with the RF reference of the machine, a jitter of 45 fs (rms) between the laser and the reference has been measured [20].

For perfect, linear compression and transport of the electron bunch, a 250 fs portion of the bunch could potentially be used for seeding. For a perfect, frequency tripled laser pulse, 100 fs could be used for seeding. Under these assumptions, synchronization is trivial. Under pessimistic, but possible assumptions about non-linear compression and transport, only 10 fs of the electron bunch and 20 fs of the laser pulse would be usable for seeding and under these conditions, neither RF synchronization nor optical cross-correlator based synchronization would be sufficient.

Reality lies somewhere between these two extremes and even small improvements in the most pessimistic assumptions bring the synchronization problem from the impossible into the possible. For example, given 25 fs (rms) synchronization, even if the portion of the electron bunch which could be seeded is only 20 fs (rms) long and the portion of the laser pulse with appropriate qualities is 40 fs (rms) long, 40% of all shots should produce overlap over at least 10 fs (rms).

A measurement of a typical electron bunch profile during an HHG experiment run is shown in Fig. 7. One sees that the seed-able portion of the bunch lies in the middle of the bunch where the charge density is high and the slice energy spread is low. Depending on the operation point of the EEHG experiment one might expect between 10 and 150 fs of the bunch to be seed-able.

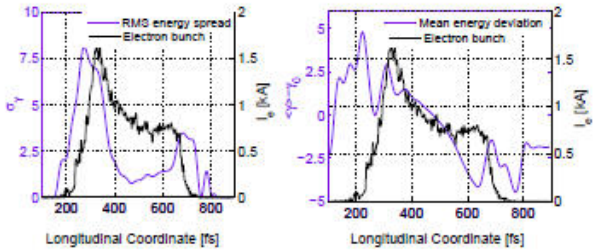

Figure 7: Longitudinal charge distribution of electron bunch plotted together with measured slice energy spread (left), and deviation of the slice energy from the nominal (right). From R. Tarkeshian et al., Proc. of PAC'11 (New York) [21].

POLARIZATION CONTROL

In an echo-seeding setup, there is a chicane in between the first and second modulator undulators. This chicane delays the electron beam relative to a seed laser by about a picosecond. To produce seed overlap with the electron beam in both undulators, one has several options

- two lasers, one delayed relative to the other
- a single laser and two laser transport lines
- a single laser where the delay is produced by inserting a dispersive material in the laser path through the chicane
- a single laser with orthogonal undulators and a birefringent crystal used to longitudinally split the laser pulse (Fig. 8)

Given a laser with sufficient pulse energy, the last of these options is the clear choice.

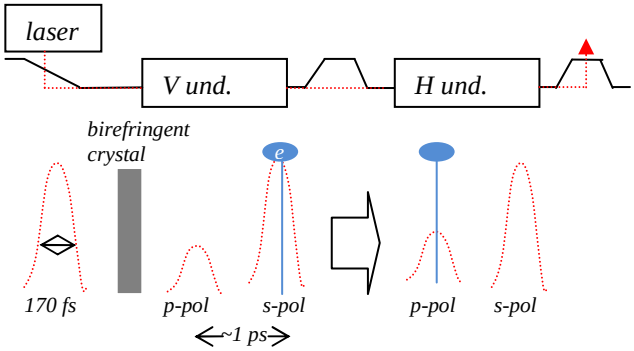

Figure 8: Generating a delay between *s* and *p* polarization splits the pulse longitudinally so that it can be used to seed in both undulators. The undulator labeled *H und.* produces horizontal oscillations and *V und.* produces vertical oscillations.

By splitting the laser pulse longitudinally using a birefringent crystal as the delay material, rotations of the crystal about the beam direction (ϕ) would change the polarization of the incoming pulse, thereby attenuating the effective electric field of the pulse in proportion to the rotation of the element. Tilting the crystal (θ) would provide a mechanism for fine-tuning the delay produced, allowing for flexibility in choosing a chicane R_{56}. The geometry of the crystal and rotations is depicted in Fig. 9.

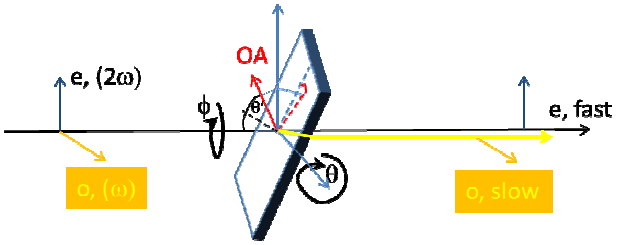

Figure 9: Rotations of a birefringent crystal about the beam direction (ϕ) change the amount of power in each polarization state and tilting the crystal (θ) produces small changes in the delay between the fast and slow pulses.

Three alpha BBO crystals were purchased with thicknesses of 1 mm, 1.25 mm and 1.5 mm. This should accommodate the range of chicane R_{56}s from 500 μm to 700 μm. Although the tilt can be used to adjust the delay over a wide range, it is better to use a crystal which is not tilted very much, due to the spatial chirp that the pulse will acquire in a tilted crystal.

In order to make sure that the *s* and *p* polarized pulses have the correct orientation with respect to the planes of electron beam oscillation in the undulators, a 1/2-waveplate is required either before or after the crystal. If it is installed prior to the crystal, its rotation determines the amount of power in the individual polarization states and the crystal rotation (ϕ) determines whether or not the polarizations of the pulses are appropriate for the undulator orientations.

A complication is added to the tuning of the power levels of the *s* and *p* polarized light due to the fact that the

- The mirrors reflect 99.6% of the *s* polarized light and only 97% of the *p* polarized light.
- The second to last mirror has a 60 degree angle of incidence and all others have 45 degree angles of incidence.

If all of the mirrors had 45 degree incidence, maintaining pure *s* and *p* reflections would be a simple matter. Due to the second to last mirror, however, one must pre-compensate for the polarization rotation that it will produce, and as a result, all reflections will have mixed polarization states, giving rise to further unwanted polarization rotations which will probably be different for the two, longitudinally separated pulses, making the two pulses less and less orthogonal. It would be preferable to have as many pure *s* and *p* reflections as possible, and rotate the polarization again as late as possible using a very thin 'true' zero-order ½-waveplate which would only need to be adjusted once. Unfortunately, it is impossible to manufacture such a 12 μm thick plate and one alternative would be to install a wave-plate as the vacuum window. A more reasonable alternative would be to use a 'true' 3rd order ½-waveplate, despite the losses which would result.

Without a zero-order waveplate after the 60 degree mirror, one can pre-compensate for the polarization rotations due to the mirror but then one should expect that rotations of the birefringent delay crystal about the z-axis will not change the power in the individual polarization states in the undulators in a purely linear fashion. Iterative tuning and calibration of the power levels in the undulators would be required.

WAVEFRONT CONTROL

An adaptive optics package involving two deformable mirrors and measurements of the 800 nm and 270 nm wavefronts will be required in order to modulate the energy of the electron bunch with sufficient quality. They will be installed prior to the tripler (out-of-vacuum) and after the tripler (in-vacuum). An example of the improvement in a laser focus produced by the application of a deformable mirror is shown in Fig. 10.

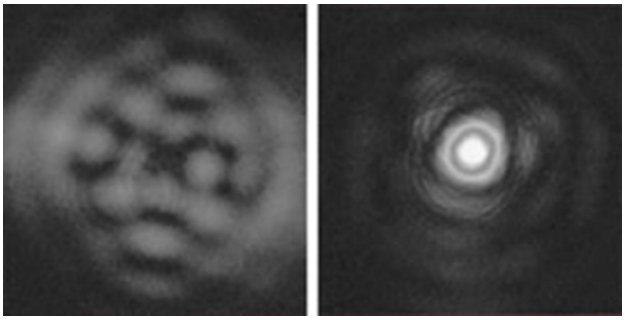

Figure 10: Beam focus before (left) and after (right) the use of wavefront tuning on the incident beam. Image taken from imagine-optic.com.

It is possible to tune such a mirror based on measurements using either screen images or direct measurements of the wavefront. Screens or wavefront sensors installed in the electron beam line or before it could all be used in a search for the most effective wavefront control, but the ultimate diagnostic will be the FEL beam itself. We will first attempt tuning the deformable mirror with a genetic algorithm using screen images as the in-loop diagnostic criteria, with a wavefront sensor as an out-of-loop diagnostic. We may also attempt the reverse configuration as well.

The quality of the 800 nm laser wavefronts has a strong influence on the efficiency of the frequency tripler. While a beam with a flat wavefront can have more than 20% conversion efficiency, a spatially distorted pulse may have less than 10% conversion efficiency. The better the conversion efficiency that we can achieve, the less input

pulse energy we would require. If we can use lower input pulse energy, we can expect less of an influence from non-linear phase shift in the several meters of air prior to the entrance to the vacuum.

The quality of the 270 nm laser wavefronts will directly translate to the quality of the echo-seeding microbunches. While small tilts of the wavefront can be compensated with adjustments of the chicane dispersion, more complicated distortions will directly degrade the bunching factor of the goal harmonic, effectively smearing out the longitudinally projected charge density.

The tolerances of seed laser wavefront distortion depend on the harmonic number one aims to achieve. For the range of harmonics around 20 the flatness required is about 2 nm (rms). For higher harmonics, the tolerances become tighter. This was investigated in [10].

These tolerances are impossible to achieve for the entire, 700 nm (FWHM) laser spot. Even if there are only lower-order distortions of the wavefront, and a deformable mirror is used for correction, the flatness that one could expect over the whole spot would be ~60 nm (rms) [23]. In fact, the best UV wavefront sensor we have found achieves an accuracy of no better than 2.5 nm [24]. It may, however, be possible to achieve a high-quality wavefront over a small region. Since we expect an electron bunch diameter of between 120 μm and 235 μm, the target tolerance should be <2 nm wavefront distortion over the central 200 nm of the 700 nm (FWHM) spot. Another iteration will involve tuning the wavefront based on a lower harmonic FEL beam. A lower harmonic will be easier to produce than a higher harmonic beam and the wavefront corrections obtained will also be applicable to the higher harmonics.

If the deformable mirrors do not provide sufficient wavefront quality, a spatial filter may be employed after the tripler in order to address microscopic distortions. This would require additional folding of the beam in the vacuum sealed boxes, so that the beam could be focused on a conical aperture at the diffraction limit. The idea is that deformable mirrors fix the macroscopic wavefront distortions and the conical aperture fixes the microscopic wavefront distortions. While these sorts of spatial filters have been employed to improve UV beams for photo-cathode injectors [25] and they can be used as an optical fuse in order to protect optics from high-power laser "hot-spots" [26], they cause significant losses in beam power, they require very low pointing jitter (fast steering feedback) and we are hopeful that the deformable mirrors alone will provide sufficient wavefront quality. If it is required, it could be installed after the initial commissioning, in September of 2012.

TRANSVERSE OVERLAP

In order to achieve transverse overlap with the electron beam, four motorized steering mirrors will be at our disposal. The first pair of steering mirrors will be in the tunnel, after the tripler and mirror-based telescope (Fig. 14). These table-mounted mirrors will be used to steer the beam for day-to-day operation. After these mirrors, there will be two more motorized steering mirrors installed in the vacuum flanges. It is intended that these flange-mounted mirrors will be adjusted one time during initial set-up and then not used for day-to-day steering of the beam. The reason for this is that there will be near-field and far-field detectors available after the table-mounted mirrors but not after the flange-mounted mirrors. With the near-field and far-field detectors used to detect the small portion of light which is transmitted through the dielectric mirrors, steering references can be generated and calibrated with references given by laser-spot images on YAG/OTR screens in the electron beam line.

Due to the 45 degree angles of incidence onto the table-mounted steering mirrors, and the gimbal mirror mounts which have been selected, it will be possible to independently adjust the angle and position of the beam. By tilting two gimbal mounted mirrors in opposite directions, a change in the position of the beam without affecting the angle of the beam can be affected. This sort of arrangement should make it easier to design an automatic steering algorithm. The orientations and mechanisms of the table mounted steering mirrors with near- and far-field detectors are depicted below in Fig. 11.

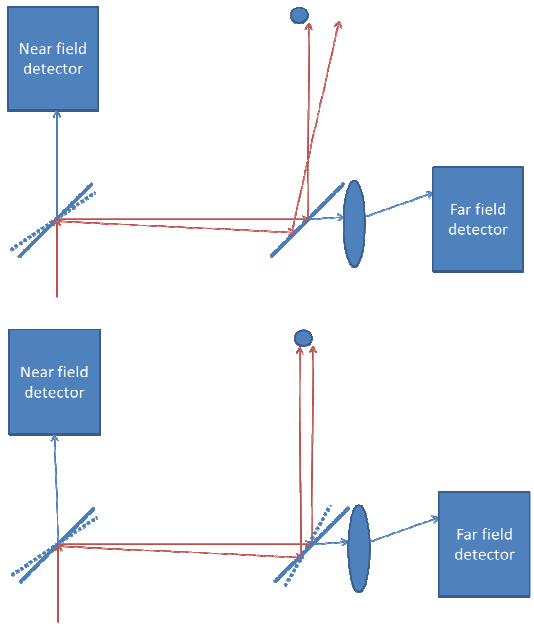

Figure 11: The table-mounted steering mirrors will transmit a small portion of the light to near- and far-field detectors. Tilting gimbal mirror mounts in opposite directions can produce changes of the beam position without affecting the beam angle.

If the lens for the far-field detector has a focal length of 20 cm, the location of the spot measured by a CCD installed at the focus of the lens will mostly sensitive to the beam angle at the second steering mirror. If the beam angle changes by a micro-radian for a 20 cm focal length lens, the spot will only move by a couple of microns. In

order to improve the far-field detector sensitivity to angle changes, the focal length of the lens would need to be larger and the detector would need to be placed further away. In principle, a focal length of even 2 meters could be used.

LONGITUDINAL OVERLAP

Several tools for finding the longitudinal overlap will be at our disposal: a streak-camera for picosecond resolution [21], optical transition radiation (OTR) screens for the detection of coherent optical transition radiation (cOTR), a TG FROG for UV laser characterization, installed near the second chicane, and LOLA, the transverse deflecting cavity for measurements of the longitudinal profile of the electron beam [27]. LOLA will be particularly useful for diagnosing changes in the energy spread of the beam due to the interaction of the electron beam with the seed laser.

The first step towards achieving longitudinal overlap would be to set up the electron beam with the fast beam arrival-time feedback [19]. One would then select the 10th bunch or so from bunch train because it will have a more stable arrival-time than those that precede it. For this 10^{th} bunch, one could then use the photodiode in the ORS chicane to find nanosecond overlap with the laser. A vector modulator is used to scan the phase of the laser relative to the machine reference. The next step would be to use the streak camera installed in the first ORS undulator to find picosecond overlap. cOTR from the OTR screen could then be used to find femtosecond overlap. In parallel, LOLA should also provide femtosecond resolution of the longitudinal overlap, due to the fact that the energy spread (width) of the beam on the LOLA screen should increase when overlap is achieved.

After overlap in at least one undulator has been achieved, one should rotate the waveplate prior to the alpha BBO delay crystal so that all laser power is in the polarization state appropriate for the first undulator. When a maximum energy spread is observed with LOLA, one would rotate the waveplate so that all of the laser power is in the polarization state appropriate for the second undulator. Then one can tune the tilt of the delay crystal as well as the R_{56} of the first ORS chicane in order to maximize the overlap in the second ORS undulator, tuning until a maximum energy spread has been observed with LOLA.

Then one can rotate the waveplate so that the ratio of the laser power in each undulator matches that which is expected by the simulation for the desired harmonic. One would then attenuate the laser power until the net energy spread measured with LOLA matches what would be expected by the simulation. The LOLA energy spread resolution is 100keV at 1GeV and should be sufficient to determine the EEHG laser power setpoint. The cOTR from the second ORS chicane screen should also be observed for evidence of laser-induced bunching.

After an appropriate amount of energy modulation has been achieved, one would then turn off the LOLA kicker and observe the radiation on the sFLASH undulator spectrum. The R_{56} of the last ORS chicane would then be tuned until seeded FEL radiation is observed. If the experiment is successful, it should be clear through a comparison of modulated pulses and non-modulated pulses. Enhanced coherence and intensity would be expected from the seeded pulses.

PARASITIC OPERATION

Parasitic operation can be restricted by either laser safety issues or incompatibility with the SASE program. Because, with appropriate interlocks, it is not possible for dangerous quantities of 270 nm or 800 nm light to make it to the viewports in the user area [9], laser interlocks for user safety will not be required and parasitic operation will not be restricted on that basis. Due to the wide range of beam energies and wavelengths that can be pursued with EEHG, as long as the beam orbit through the ORS and sFLASH section is reasonable, the orbit should not be an impediment to parasitic operation. It has also been determined that the incoming microbunching instability would only be exacerbated by the ORS section when the undulators are tuned to radiate at wavelengths which are well above the 270 nm wavelength which will be used for EEHG [9]. The main disturbance which could be posed by the EEHG experiment would be the request to insert screens in order to tune the overlap with the electron bunch. Given the near and far-field detectors in the laser transport line, the laser can be steered to a known reference trajectory without inserting screens in the electron beamline. In this way, the screens would only be required for initial calibration of the near and far-field detectors and as a final cross-check of the parasitic alignment procedures. With automation of the transverse overlap process, it should not take more than a few minutes of beam time per shift.

CONCLUSION

Using the undulators and chicanes developed for an optical replica synthesizer (ORS) experiment together with the sFLASH 800 nm seed laser, radiator undulators and diagnostics, an echo-seeding experiment will be conducted at FLASH in January 2012. For this experiment, a 130 fs (FWHM) 800 nm laser pulse will be transported with a new, 12 meter long, in-vacuum laser transport line. On an in-vacuum optical breadboard, the 800 nm pulses will then be frequency tripled in beta-BBO nonlinear crystals. The 270 nm laser pulse will then be split longitudinally using a birefringent alpha-BBO crystal into two pulses with orthogonal polarization states corresponding to the orthogonal orientations of the ORS undulators. These pulses will be focused to a 700 um (FWHM) waist between the undulators with a Galilean telescope and then steered with 4 motorized mirrors onto the electron beam axis in the ORS undulator section. LOLA and cOTR will be used to diagnose the bunching of the beam prior to the sFLASH section.

ACKNOWLEDGEMENTS

Thank you to Josef Gonschior (DESY) for the design, drawings and construction work. This work was supported by DESY, BMBF 05K10PE1, and grant 621-2009-2926 of the Swedish research council.

REFERENCES

[1] D. Xiang and Stupakov, *Echo-enabled Harmonic Generation for Free Electron Lasers*, SLAC-PUB-13474, Dec 2008.

[2] G. Stupakov, *Using the Beam-Echo Effect for Generation of Short Wavelength Radiation*, PRL.102.074801 2009.

[3] E. Allaria, et al., *Echo Enhanced Harmonic Emission in FERMI*, Proc. of FEL'09 (Liverpool).

[4] S. Reiche, et al. *Echo Enabled Harmonic Generation Scheme for SWISSFEL*, Proc. of FEL'09 (Liverpool).

[5] H. Deng, et al., *The Echo-Enabled Harmonic Generation (EEHG) Options for FLASHII*, FLASH Seminar December 06, 2010.

[6] D. Xiang et al., *Demonstration of the Echo-Enabled Harmonic Generation Technique for Short-Wavelength Seeded Free Electron Lasers*, PRL, 105, 114801 (2010).

[7] Z. T. Zhao et al., *Progress in SDUV-FEL and Development of X-Ray FELs in Shanghai*, proceedings of the 2010 Proc. of FEL'10 (Malmoe).

[8] K. Hacker, et al., *New Uses for the ORS Section at FLASH*, TESLA-FEL 2011-03.

[9] K. Hacker, et al., *Parasitic Operation of the ORS Section at FLASH*, TESLA-FEL 2011-04.

[10] K. Hacker, et al., *Tolerances for Echo Seeding in the FLASH ORS Section*, TESLA-FEL 2011-05.

[11] J. Hollar, DESY personal communication.

[12] Wikipedia page on Self-Focusing.

[13] Gaeta, A. L. "Catastrophic Collapse of Ultrashort Pulses", Phys. Rev. Lett. 84, 3582 (2000)

[14] Fibich, G. and Gaeta, A. L. "Critical power for self-focusing in bulk media and in hollow waveguides", Opt. Lett. 25, 335 (2000)

[15] Nibbering, E.T.J. et al. "Determination of the inertial contribution to the nonlinear refractive index of air, N2, and O2 by use of unfocused high-intensity femtosecond laser pulses", J. Opt. Soc. Am. B 14, 650 (1997)

[16] Garcia, H. et al. "New approach to the measurement of the nonlinear refractive index of short (<25 m) lengths of silica and erbium-doped fibers", Opt. Lett. 28 1796 (2003)

[17] SNLO nonlinear optics code from A. V. Smith, AS-Photonics, Albuquerque, NM, USA.

[18] W. Koprek, et al., *Intra-train Longitudinal Feedback for Beam Stabilization at FLASH*, Proc. of FEL'10 (Malmoe).

[19] S. Schultz, et al., *Progress and Status of the Laser-based Synchronization System at FLASH*, Proc. of DIPAC 2011 (Hamburg).

[20] M. Felber, et al., *RF-based Synchronization of the Seed and Pump-probe Lasers to the Optical Synchronization System at FLASH*, Proc. of FEL'10 (Malmoe).

[21] R. Tarkeshian, et al., *Femtosecond Resolved Determination of Electron Beam and XUV Seed Pulse Temporal Overlap in sFLASH*, Proc of PAC'11 (New York).

[22] G. Vdovin, et al., *Correction of low order aberrations using continuous deformable mirrors*, Optics Express 16, 2859-2866 (2008).

[23] E. Dalimier, et al., *Comparative analysis of deformable mirrors for ocular adaptive optics*, Optics Express 13, 4275-4285 (2005).

[24] Specifications for HASO UV Hartmann sensor.

[25] SWISSFEL injector design.

[26] www.imagine-optic.com/applications, *Next Generation Optical Fuse.*

[27] Michael Roehrs, "Investigations of the Phase Space Distribution of Electron Bunches at the FLASH-Linac Using a Transverse Deflecting Structure", DESY-THESIS-2008-012, 200.